

## REPORT DOCUMENTATION PAGE

Public reporting burden for this collection of information is estimated to average 1 hour per response, including gathering and maintaining the data needed, and completing and reviewing the collection of information. Send comments regarding this burden estimate or any aspect of this collection of information, including suggestions for reducing this burden, to Washington Headquarters Services, Directorate for Information Operations and Reports, 1215 Jefferson Davis Highway, Suite 1204, Arlington, VA 22202-4302, and to the Office of Management and Budget, Paperwork Reduction Project (0704-0188), Washington, DC 20503.

<b>1. AGENCY USE ONLY (Leave blank)</b>		<b>2. REPORT DATE</b> March 16, 1997	<b>3. REPORT TYPE AND DATES COVERED</b> Final Technical Report 01 Jul 94 to 31 Dec 97	
<b>4. TITLE AND SUBTITLE</b> Unsteady Loads on Compressor and Turbine Blade Induced by Passage of a Density Wake			<b>5. FUNDING NUMBERS</b> F49620-94-1-0202	
<b>6. AUTHOR(S)</b> B. Ramer S. Wijesinghe C. Tan & E. Covert				
<b>7. PERFORMING ORGANIZATION NAME(S) AND ADDRESS(ES)</b> Center for Aerodynamic Studies Department of Aeronautics & Astronautics Massachusetts Institute of Technology			<b>8. PERFORMING ORGANIZATION REPORT NUMBER</b>  R-98-003	
<b>9. SPONSORING/MONITORING AGENCY NAME(S) AND ADDRESS(ES)</b> AFOSR/NA 110 Duncan Avenue, Suite B115 Bolling AFB, DC 20332-8050			<b>10. SPONSORING/MONITORING AGENCY REPORT NUMBER</b>  F49620-94-1-0202	
<b>11. SUPPLEMENTARY NOTES</b>				
<b>12a. DISTRIBUTION AVAILABILITY STATEMENT</b> Approved for public release; distribution unlimited.			<b>12b. DISTRIBUTION CODE</b>	
<b>13. ABSTRACT (Maximum 200 words)</b> <p>The object of the research funded under this grant is to study the unsteady aerodynamic forces and moments induced on cascade blades by a convected density gradient that is more or less normal to the flow path. Previous investigators have considered the effect of a variety of convected disturbances on cascade, compressor, and turbine performance. However, we believe this is the first investigation to focus on the production of unsteady loads associated with this process.</p> <p>The size and frequency content of these loads, when combined with other loads as fan, compressor and turbine blades have the potential to reduce the blade's high cycle fatigue life.</p>				
<b>14. SUBJECT TERMS</b> Unsteady Blade Loads, Wake Convection in a Blade Passage			<b>15. NUMBER OF PAGES</b> 39	
			<b>16. PRICE CODE</b>	
<b>17. SECURITY CLASSIFICATION OF REPORT</b> Unclassified	<b>18. SECURITY CLASSIFICATION OF THIS PAGE</b> Unclassified	<b>19. SECURITY CLASSIFICATION OF ABSTRACT</b> Unclassified	<b>20. LIMITATION OF ABSTRACT</b> UL	

19980514 102

DTIC QUALITY INSPECTED

24 MAR 1998

Final Report<sup>gd</sup>  
on  
AFOSR GRANT F49620-1-0202

Principal Investigator: Eugene E. Covert

Research on  
Unsteady Airloads due to Density Gradients

Center for Aerodynamic Studies  
Department of Aeronautics & Astronautics  
Massachusetts Institute of Technology

March 16, 1998

## Objective

The object of the research funded under this grant is to study the unsteady aerodynamic forces and moments induced on cascade blades by a convected density gradient that is more or less normal to the flow path. Previous investigators have considered the effect of a variety of convected disturbances on cascade, compressor, and turbine performance. However, we believe this is the first investigation to focus on the production of unsteady loads associated with this process.

The size and frequency content of these loads, when combined with other loads as fan, compressor and turbine blades have the potential to reduce the blade's high cycle fatigue life.

## Objectives Reached

Since the basis for the research is to conduct a set of parametric experiments, the first essential factor is to validate CFD codes. This work was completed and we have used the following codes in operation:

- (1) Modified Valkowitz - incompressible inviscid code
- (2) Modified Hoying - compressible viscous code - both laminar and k- $\epsilon$  turbulence

With these two codes in operation we have studied the following cases.

### A. Incompressible - inviscid flow

$w/c \backslash \rho^*$	-2/3	-1/3	-1/6	-1/9	1/9	1/6	1/3
0.1	x o	x o	x		x	x	x
0.2		x o			x	x o	
0.4	x	x		x	x	x	x
0.6					x		

**Table 1:** Calculation matrix for sinusoidal density wakes. x = NACA4F blade row calculations, o = EEE blade row calculations.

Some additional cases have been run for a flat topped wake.

- B. Compressible - Turbulent Flow,  $M = 0.15$
- C. Compressible - Turbulent Flow,  $M = 0.53$

### New Findings\*

Over the period of this grant a set of numerical results have been obtained for flow of a turbulent compressible fluid through a cascade. These results show the unsteady loads have the form for Mach numbers up to at least 0.53 and Reynolds numbers of 267,000.

$$\frac{\Delta C_Y}{C_Y} = (K_1(\frac{w}{c})\rho^*)\sqrt{1-M_\infty^2} \quad \text{and} \quad \frac{\Delta C_M}{\psi C_M} = (K_2(\frac{w}{c})\rho^*)\sqrt{1-M_\infty^2}$$

where

$C_Y$  = azimuthal force as a rotating blade

$C_M$  = torque about the midchord axis

$\Delta()$  = peak unsteady loading with respect to mean

$M_\infty$  = inlet Mach number

$\frac{w}{c}$  = width of disturbances normalized with respect to the chord

$$\rho^* = \frac{\rho_2 - \rho_1}{\rho_2 + \rho_1}$$

= normalized density change

$\rho_1$  = density before change

$\rho_2$  = peak value (of density change, may be maximum or minimum)

Note:  $\rho^*$  may be as large as 0.5 for cooled turbine blades and is of the order - 0.15 for compressors with a blade at the adiabatic wall temperature.

$\psi$  = pressure ratio

$K_1$  and  $K_2$  are constants that depend upon blade geometry and loading, whose relation to  $\psi$  and blade separation remains to be explored.

We have also conducted calculations with the modified Hoying Navier-Stokes code. The results show that near the design point the results from the compressible calculations and the calculations with a turbulent boundary layer

---

\*See attached summary report for technical details.

agree very well with the incompressible, inviscid results if  $\rho^* \leq 0.20$  for  $M = 0.53$ . The difference between the two sets of calculations is larger as the product  $\frac{w}{c} \rho^*$  is larger. In other words for larger disturbances, the process is increasingly non-linear, particularly as  $\rho^* > 0^1$ .

Wake Parameters	%ΔCy / Cy (mean)		%ΔCm / [ψ Cm (mean)]	
	Inviscid	Viscous	Inviscid	Viscous
w/c = 0.1 ρ* = -0.60	-14.0	-13.3	-77.4	-58.5
w/c = 0.1 ρ* = -0.33	-7.8	-7.2	-43.0	-35.9
w/c = 0.1 ρ* = -0.14	-3.3	-3.8	-18.4	-17.0
w/c = 0.2 ρ* = -0.60	-25.2	-21.6	-120.5	-94.6
w/c = 0.2 ρ* = -0.33	-14.0	-12.3	-66.9	-53.3
w/c = 0.2 ρ* = -0.14	-6.0	-5.5	-28.7	-26.9

**Table 2: Comparison of inviscid and viscous results. Percentage changes in unsteady peak load and moment response is shown.**

In this calculation a minus sign implies the unsteady loading is in the opposite direction to mean load.

Figure 1 shows the effect of the density gradient for  $\rho_2 < \rho_1$ . The perturbation velocity field is shown in Figure 2 and typical unsteady time-load curves are shown in Figure 3.

The effect of the density wake is to generate a pair of vortices of opposite sign. They are located ahead and behind the wake.

This picture suggests a model of a convected vortex pair. Such a model has been developed and is very useful. For example the small bump in Figure 3a and 3b is the consequence of the trailing vortex being formed at the leading edge. This bump is bigger as the wake is narrower, i.e.  $\frac{w}{c}$  is smaller.

These findings show the objective of the research has been met.

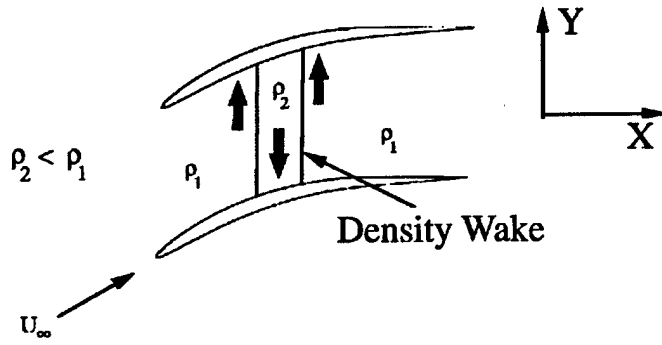


Figure 1: Density wake convecting through a blade passage.

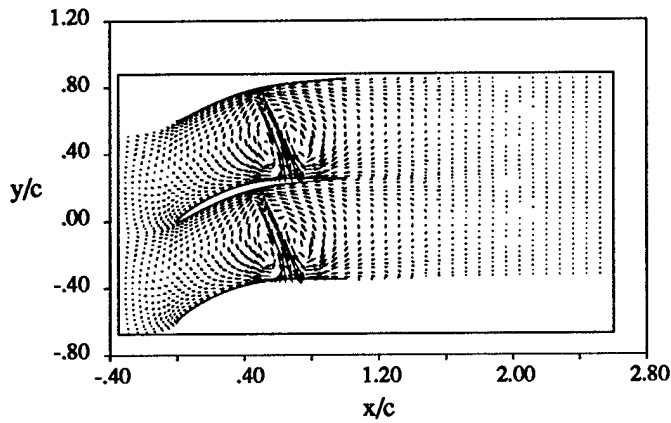


Figure 2: Perturbation velocity vectors for sinusoidal density wake with  $\rho^* = -1/3$  and  $w/c = 0.2$ .

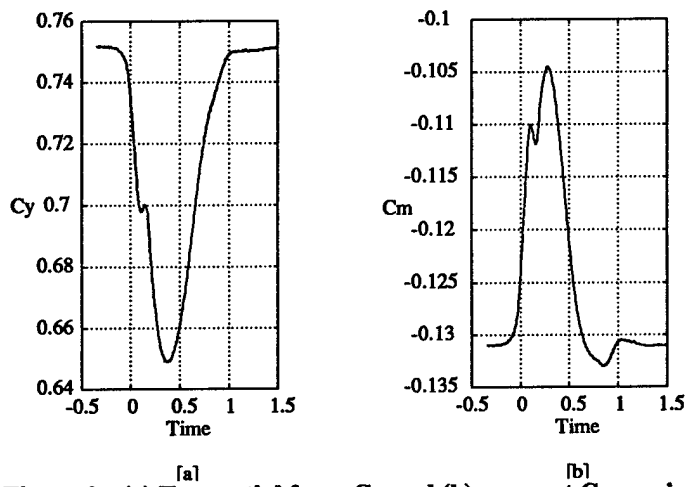


Figure 3: (a) Tangential force  $C_y$  and (b) moment  $C_m$  variation on NACA4F blade during passage of a sinusoidal density wake with  $\rho^* = -1/3$  and  $w/c = 0.2$ .

Further these findings would seem to have two practical consequences. The first is that the density wake can provide an additional unsteady force and moment on the blade. A second finding is that the density wake flow field suggests an altered heat transfer load on turbine blades.

The potential application to the design of Air Force and civil gas turbine engines lies in the refinement of the unsteady loads, and their effect on the design margin.

The U.S. Air Force has and continues to encounter serious problems with high cycle fatigue in components of gas turbine engines. High cycle fatigue failures occur after a part is subjected to many, perhaps a million per flight hour (or more), cycles of unsteady loads. These cyclic loads interact with the blade dynamics and change the load profile under some circumstances. A change in the material properties, can lead to formation of cracks, and ultimately failure of a part. This problem is commonly encountered in Gas Turbine engines.

As a consequence the number of engines needed to insure a mission ready squadron is larger than would be needed if high cycle fatigue failures could be avoided. In addition to the difficulties faced in maintaining a mission ready force, additional resources, both in labor hours and spare parts, are needed. Clearly, high cycle fatigue failures in gas turbine engines place an extra burden on the Air Force at a time when resources are limited.

Hence understanding and reducing the severity of this burden through understanding the broad phenomena of unsteady loads, blade dynamics and material properties, and their coupling is of value to the Air Force.

#### Personnel Supported

T. Wilson Professor, Emeritus	Dr. Eugene E. Covert	(MIT)
Principal Research Associate	Dr. Choon Tan	(MIT)
Research Assistant	Ms. Becky Ramer	(MIT)
(up to January 1997)		
Research Assistant	Mr. H. Sanith Wijesinghe	(MIT)
(Jan. 1997 - Jan. 1998)		
Consultant	Dr. Frank Marble	(Professor Emeritus, CalTech)

#### Peer Review Papers Accepted

Aerodynamic Response of Turbo Machinery Blade Rows to Convecting Density Wakes.

### **Interactions and Transitions**

Professor Covert	USAF Aero Prop. Div. Jan. '97 (SAB Review) USAF F-119 Ex. Review Group Sept. '96, Feb. '97 USAF ALC Review Group Nov. '96, Feb. '97 USAF F-22 Flight Readiness Rev. Feb. '97
Dr. Tan	Dr. Robert Kieb of G.E. Mar. '97, Sept. '97  Lectures on Introduction to Nov. '97 Aeromechanics at P & W, E. Hartford, CT & West Palm Bch, FL  with Dr. Om Shara of Pratt; Feb. '98 Lecture on Unsteadiness Induced by Blade Row Interactions in Compressors given at VKI

**No Patent or Discoveries**

**No Awards**



## Nomenclature

### Variables

$c$	Blade chord length
$h$	Blade spacing
$p$	Static pressure
$t$	Time
$u, U$	Axial velocity
$w$	Width of wake
$x$	Axial direction coordinate
$y$	Azimuthal direction coordinate
$C_m$	Moment coefficient about midchord
$C_x$	Axial force coefficient
$C_y$	Azimuthal force coefficient
$M$	Mach number
$Re$	Reynolds number based on chord $c$ and inlet total velocity
$\alpha$	Angle of attack, angle between flow and axial direction
$\lambda$	Position of density jump
$\rho$	Density
$\Psi$	Blade loading parameter
$\eta$	Coordinate normal to flat plate
$\omega$	Vorticity

### Subscripts

1	Freestream or initial value
2	Perturbation value, inside of density wake
	After density change for Marble's analysis
$\infty$	Freestream value

### Operators and Modifiers

$\tilde{()}$	Non-dimensionalized quantity
--------------	------------------------------

# 1 Introduction

High cycle fatigue (HCF) failure continues to be a serious problem in components of modern military gas turbine engines. The U.S. Air Force claims that 50% of their total irrecoverable in-flight engine shutdowns are related to high cycle fatigue. HCF failure clearly places a huge burden on maintaining a mission ready force.

Increased operational requirements and increased thrust to weight ratios have led to higher mean stress in turbine, compressor and fan blades which in turn have increased the likelihood of encountering high cycle fatigue failure. At the same time it is not clear that sources of all the unsteady aerodynamic loads have been properly studied. The purpose of the research funded under this grant is to study the unsteady aerodynamic forces and moments induced in compressor cascade blades by convected density gradients.

The effects of viscous wakes (Kemp [4]) and Kerrebrock [5] and potential flow interactions (Manwaring [6]) on compressor performance have been studied however convecting wakes and density gradients have not been considered previously as a source of unsteady loads.

While turbine blades are subjected to larger density non-uniformities (due to hot-streaks from the combustor and from blade cooling), compressor blades are considered in this study since they are more susceptible to high cycle fatigue failure.

The purpose of this research is to clarify density wake induced load phenomena. Ultimately the aeroelastic effects must be computed, but this aspect of the high cycle fatigue problem is not studied here.

In the material to follow a physical description of the origin of density wake induced forces is given. This is followed by a theoretical background which includes the derivation of non-dimensional scaling relationships for blade load fluctuations. The subsequent sections outline the inviscid and viscous results for the unsteady force and moment response.

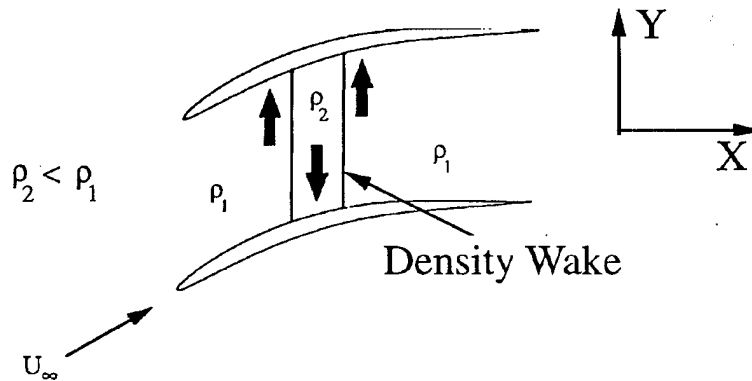


Figure 1: Density wake convecting through a blade passage.

## 2 Physical Origin of Unsteadiness

An analogy to the passage of a density wake through a compressor blade row can be found in the atmosphere; low density (high temperature) air rises to higher altitudes where the pressure is lower and remains there because of force equilibrium. Similarly, high density (low temperature) air sinks to regions of high pressure nearer to the earth.

Now consider the passage of a density wake through a cascade blade row as illustrated in Figure 1. Assume the wake has a lower density than the freestream density. As the wake moves through the blade passage, the low density fluid migrates towards the low pressure, suction side of the blade. To satisfy continuity across the wake the surrounding higher density fluid is subsequently displaced towards the pressure side of the blade. The relative motion of the low and high density fluids produce a pair of counterrotating vortices in the passage which results in a flux of material  $\rho_2$  directed toward the suction side of the blade. The counterrotating vortices therefore influence the elemental vortices which define the potential flow field around the airfoil. Hence as the density wake convects through the blade row the vorticity associated with the blade and consequently the blade loading will change with time.

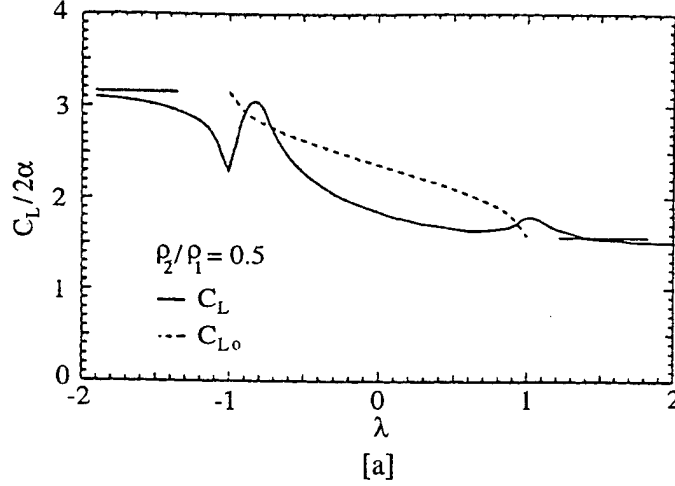


Figure 2: Lift coefficient fluctuation during passage of a density discontinuity over a flat plate.  $\lambda$  is the position of the density change as it convects along the flat plate.

### 3 Theoretical Background

Vorticity is generated by the interaction of the wake density gradient with the pressure field of the blade row. For a continuous density distribution in two-dimensional flow this vorticity satisfies the linearized relation

$$\left( \frac{\partial}{\partial t} + U \frac{\partial}{\partial x} \right) \omega = \frac{1}{\rho^2} \nabla p \times \nabla \rho \quad (1)$$

If the density gradient ( $\nabla \rho$ ) is large (zeroth order), the convected vorticity  $\omega$  is of the same mathematical order as the pressure field of the airfoil [7].

The first study of density gradients as a source of flow unsteadiness was conducted by Marble [7]. He performed a linearized potential flow analysis for a flat plate at angle of attack encountering a sharp density jump (discontinuity). If the fluid is treated as incompressible and the velocity disturbances caused by the airfoil are small compared to freestream velocity, the density field can be expressed as  $\rho(x - Ut, y)$  (Marble [7]). The results of Marble's analysis are shown in Figure 2 and Figure 3. In these Figures  $\lambda$  is the position of the density change as it convects along the flat plate which lies between  $|\lambda| \leq 1$ .

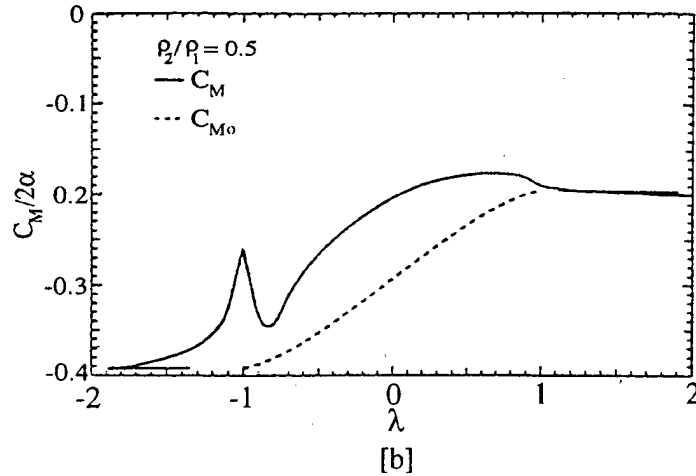


Figure 3: Moment coefficient fluctuation during passage of a density discontinuity over a flat plate.  $\lambda$  = position of density discontinuity as it convects along the flat plate.

The dotted lines correspond to the quasi-steady results while the solid lines correspond to the unsteady results. Initially the effect of the density change is to reduce the local lift. This is a consequence of a downwash field which precedes the arrival of the density jump [7]. This is followed by a rapid rise in lift as the density jump convects across the leading edge. This is caused by an upwash field behind the density jump. A gradual relaxation of the perturbation occurs as the density change convects further aft. The final steady lift scales with the ratio of density across the jump. The moment coefficient, Figure 3, also reflects these events in local loading.

Marble's linearized analysis provided a basic understanding of the parameters involved in this problem. In particular, the density parameter  $\rho^*$ ,

$$\rho^* = \frac{\rho_2 - \rho_1}{\rho_2 + \rho_1} \quad (2)$$

was shown to be a key parameter in this flow field. Since scaling parameters are important and useful in engineering and scientific evaluations, a dimensional analysis of new problems is essential. Hence re-writing Equation 1 using the non-dimensional vorticity  $\tilde{\omega} = \omega w / U_\infty$ ,

$$\frac{D\tilde{\omega}}{D\tilde{t}} = \frac{c^2}{wh} \rho^* \left[ \frac{1}{\rho^2} \left( \tilde{\nabla}_w \tilde{\rho} \times \tilde{\nabla}_h \tilde{p} \right) \right] \quad (3)$$

where,

$$\begin{aligned} \tilde{p} &= \frac{p}{(\rho_2 - \rho_1)U_\infty^2} \\ \tilde{t} &= \frac{U_\infty}{c} t \\ \tilde{\rho} &= \frac{\rho}{\rho_1 + \rho_2} \\ \tilde{\nabla}_w &= w \nabla \\ \tilde{\nabla}_h &= h \nabla \end{aligned}$$

suggests parameters  $w/c$  and  $h/c$  (non-dimensional wake width and blade spacing) as additional key variables.

## 4 Technical Approach

Two-dimensional, inviscid numerical simulations of the flow through a cascade were conducted initially to gain a basic understanding of the flow physics in the absence of boundary layer interactions. The temporal variations in force and moment caused by passage of a single density wake were quantified and the dimensionless parameters which govern the loading variations were determined. Viscous simulations were then performed at both incompressible ( $M_\infty = 0.15$ ) and compressible ( $M_\infty = 0.53$ ) speeds to assess the impact of the boundary layer and compressibility on the force and moment coefficients. The non-dimensional wake width and density parameter were used as parametric variables for all tests. The non-dimensional cascade blade spacing however was kept constant for all tests in this study.

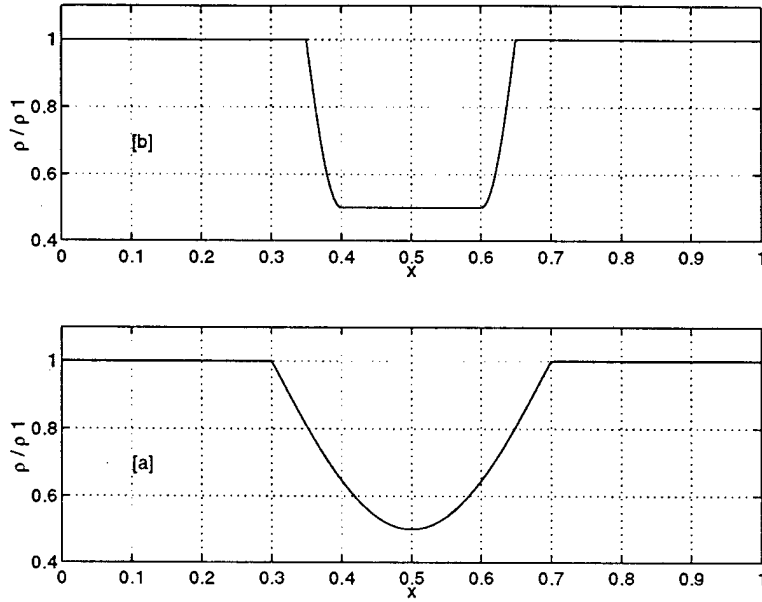


Figure 4: Wake density distributions. (a) Sinusoidal and (b) flat top distributions starting from freestream density  $\rho_1$  to peak density  $\rho_2$  and back again to freestream density  $\rho_1$ .

## 5 Inviscid Results

An incompressible two-dimensional, spectral element solver written and utilized by Valkov [12] was used for the inviscid calculations. The spectral element solver computes the flow through the blade passages governed by the Navier Stokes equations. In order to obtain inviscid solutions the viscosity was set to zero and a slip boundary condition was prescribed on the blade surface. This boundary condition removes the blade surface boundary layer and effectively simulates inviscid flow conditions. A detail description of the numerical method is provided by Valkov and is not reproduced here. Additional description of the computational domain is provided by Ramer [8]. The inviscid flow results presented below are taken from Ramer, et.al. [10]

### 5.1 Wake Model

The density wake used for this study is a planar disturbance normal to the blade. Two different distributions of density are studied. The first distribution shown in Figure 4b will be referred to as a “flat top” wake. The

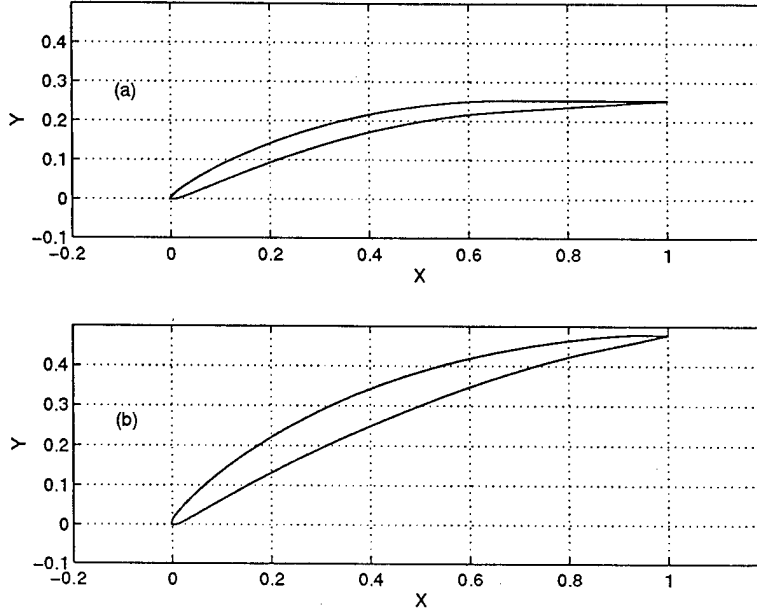


Figure 5: Compressor blade geometries: (a) NACA4F blade with loading  $\Psi = 0.31$  and (b) EEE blade with loading  $\Psi = 0.50$ .

flat top wake has a sinusoidal density change from  $\rho_1$  to  $\rho_2$  then remains at the peak density  $\rho_2$  for a specified distance and finally returns sinusoidally to the freestream density  $\rho_1$ . The second distribution shown in Figure 4a has a sinusoidal density variation from freestream density  $\rho_1$  to a peak density  $\rho_2$  and then back to freestream density  $\rho_1$ .

## 5.2 Calculation Matrix

Inviscid tests were conducted on the two blade geometries shown in Figure 5; a low loaded NACA4F blade and a higher loaded EEE blade (Wisler [13]). The blade chord/spacing ratio and inlet flow angle were held constant at 1.66 and 45 degrees respectively in all tests.

Each test is characterized by a single wake convecting normal to the blade row. The combination of wake widths and density parameters used for the sinusoidal wake calculations are tabulated in Table 1.

Calculations with flat top wakes were run only for the NACA4F blade row. These wakes have  $\rho^* = 1/9$  and  $w/c = 0, 0.2, 0.6, 0.8, 1.3$  and  $1.6$ .



$w/c$ $\rho^*$	-2/3	-1/3	-1/6	-1/9	1/9	1/6	1/3
0.1	XO	XO	X		X	X	X
0.2		XO			X	XO	
0.4	X	X		X	X	X	X
0.6					X		

Table 1: Calculation matrix for sinusoidal density wakes. X = NACA4F blade row calculations, O = EEE blade row calculations.

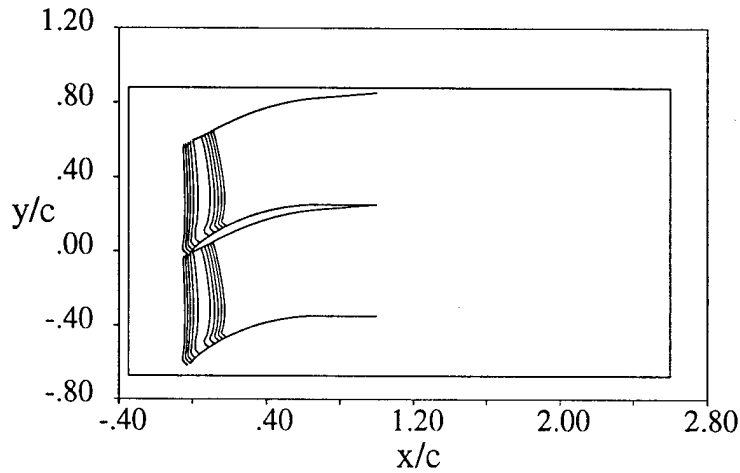


Figure 6: Plot of constant density contours showing position of the density wake at  $t = 0.15$  ( $\rho^* = -1/3$  and  $w/c = 0.2$ ).

Note,  $w/c$  for the flat top wakes correspond to the width of the flat top region only. Hence a flat top wake width  $w/c = 0.0$  corresponds to a sinusoidal wake width of  $w/c = 0.1$ .

Before examining the results of induced loading, the general physics of the flow field will be reviewed by examining the evolution of a density wake as it convects through a blade passage.

### 5.3 Evolution Of The Density Wake In Inviscid Flow

Figure 6 through Figure 8 show the evolution of a sinusoidal density wake ( $w/c = 0.2$  and  $\rho^* = -1/3$ ) as it convects through a blade passage. Time

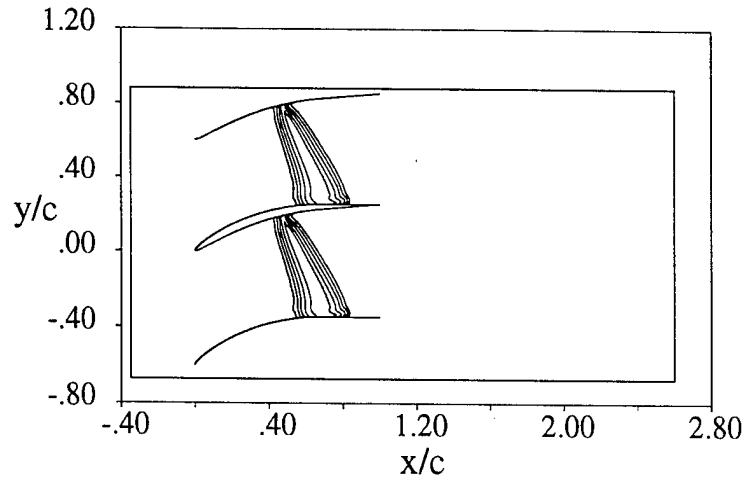


Figure 7: Plot of constant density contours showing position of the density wake at  $t = 0.65$  ( $\rho^* = -1/3$  and  $w/c = 0.2$ ).

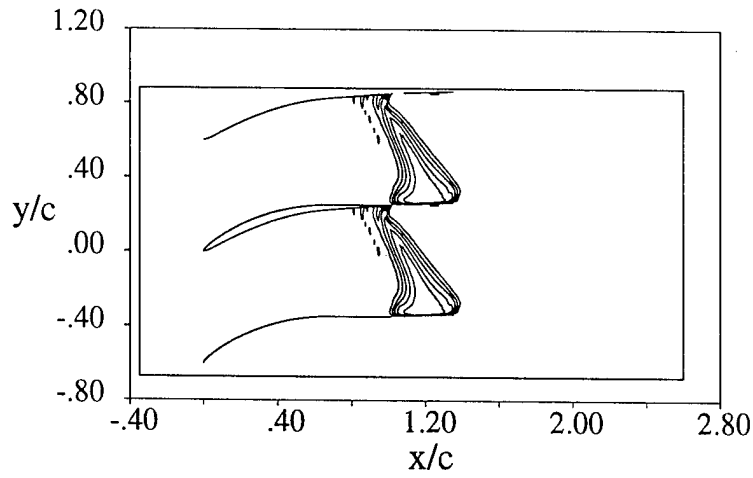


Figure 8: Plot of constant density contours showing position of the density wake at  $t = 1.15$  ( $\rho^* = -1/3$  and  $w/c = 0.2$ ).

for these inviscid tests are normalized so that  $t = 0.0$  corresponds to the wake encountering the leading edge of the blade row. The density wake is introduced at the inlet to the computational domain at  $x/c = -0.35$  (where  $x/c = 0.0$  corresponds to the leading edge of the blade). To first order the wake convects at freestream velocity.

As the density wake encounters the blade row it interacts with the blade pressure gradient and causes a local change in vorticity according to Equation 1. The resultant perturbation velocity alters the shape of the density wake as it flows through the blade passage. Figure 6 shows the density wake at a time  $t = 0.15$ . Here the density wake has been cut by the blade row, but still retains its planar shape. Figure 7 shows the wake at a later time  $t = 0.65$ . At this point the density wake shape has been altered due to equilibrium conditions in the passage. The low density fluid in the wake has traveled toward the suction side of the blade. In Figure 8 the wake has left the blade trailing edge at a time  $t = 1.15$ . The planar wake has clearly distorted during its passage through the blade row. The basic convection process causes the velocity near the suction surface to be higher than at the pressure surface. This effect combined with the natural velocity gradient across the blade row skews the wake counterclockwise as it traverses the passage. Due to convection of the less dense fluid material toward the blade suction surface, the wake has a greater width at the suction side of the blade row than at the pressure side. Ultimately the density wake changes from a planar shape to a "blob" of non-uniform density.

Wakes with larger density gradients (smaller width for given  $\rho^*$ ) deform more quickly since the stronger vorticity field increases the vertical convection of the wake material.

The response for a wake with a density increase,  $\rho^* > 0$  is similar except the wake migrates toward the pressure side of the blade row instead of the suction side. For  $\rho^* > 0$  wake skewness and wake distortion are also reduced since the induced velocities are directed opposite to the natural velocity gradients in the flow field.

The flow behavior during the passage of the density wake can be further visualized with the aid of the perturbation velocity field. The velocity vectors shown in Figure 9 clearly indicate the pair of counterrotating vortices formed along either side of the density wake at time  $t = 0.65$ .

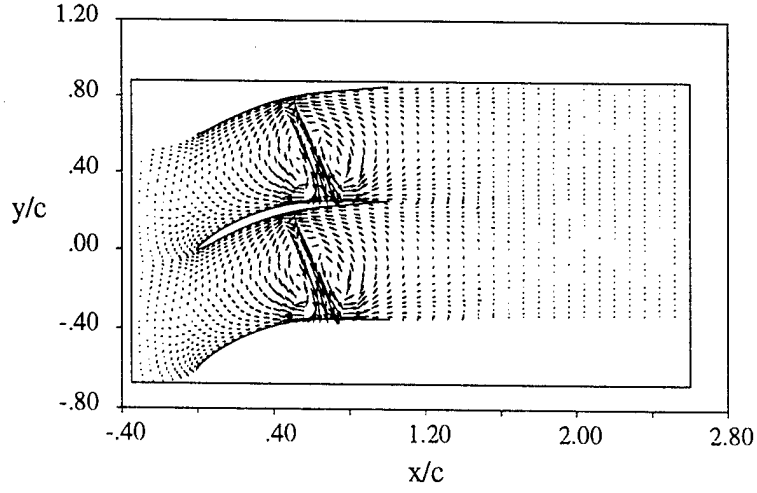


Figure 9: Perturbation velocity vectors for sinusoidal density wake ( $\rho^* = -1/3$  and  $w/c = 0.2$ ) at time  $t = 0.65$ .

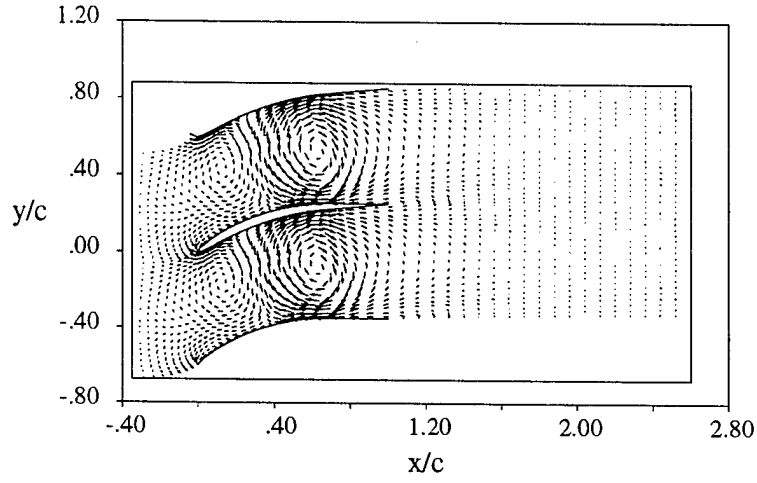


Figure 10: Perturbation velocity vectors for sinusoidal density wake ( $\rho^* = 1/6$  and  $w/c = 0.6$ ) at time  $t = 2.00$ .

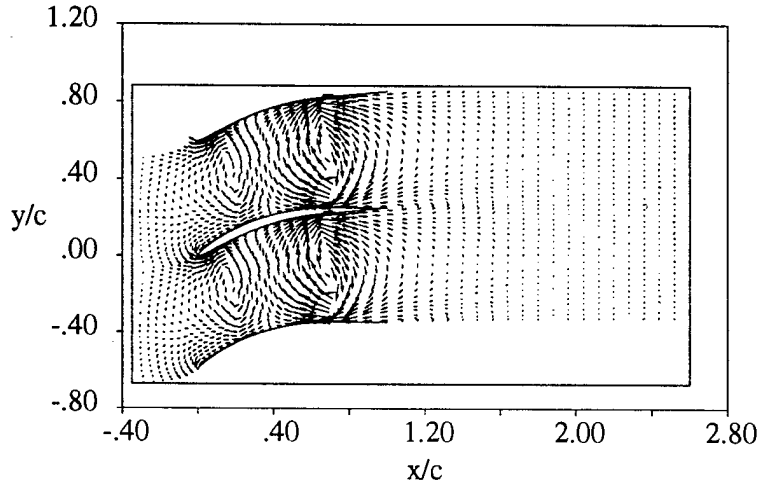


Figure 11: Perturbation velocity vectors for flat top density wake ( $\rho^* = 1/6$  and  $w/c = 0.6$ ) at time  $t = 2.00$ .

An anticlockwise vortex is formed at the leading edge of the wake and a clockwise vortex at the trailing edge of the wake. This results in a flux of fluid towards the blade suction surface.

The magnitude and rotational direction of the vortex pair depends upon the magnitude and direction of both the density gradient and the pressure gradient (Equation 1). A density wake with  $\rho^* > 0$  (internal density higher than freestream density) generates vortices which rotate in opposite direction to vortices generated by wakes with  $\rho^* < 0$ . This is illustrated in Figure 10 which shows perturbation velocity vectors generated by a very wide wake with  $\rho^* = 1/6$  at time  $t = 2.00$ . In this case the fluid flux is directed towards the blade pressure surface instead of the blade suction surface.

Higher density gradients create stronger vortex pairs. A wide flat top wake with the same  $\rho^*$  and  $w/c$  as a sinusoidal wake generates a stronger vortex pair on account of the higher density gradient along the wake leading and trailing edges as shown in Figure 11. The relative strength of the vortices can be observed by comparing the relative sizes of the perturbation velocity vectors.

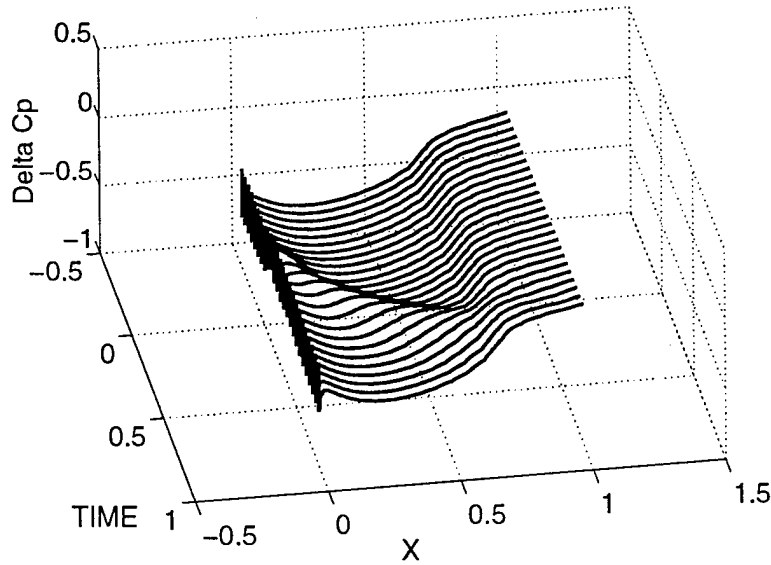


Figure 12: Difference in static pressure between suction and pressure surfaces (Delta  $C_p$ ) during passage of a density wake ( $w/c = 0.2$ ,  $\rho^* = -1/3$ ). X corresponds to distance along the blade and TIME is the convective time scale.

In addition to the strength and orientation of the vortices, the relative position of the vortex centers is also an important variable. The separation of the vortex centers is dependent on the width of the density gradient. This is illustrated by comparing Figure 9 ( $w/c = 0.2$ ) and Figure 10 ( $w/c = 0.6$ ). For a prescribed density distribution, larger wake widths will cause larger separation between the vortex centers.

The passage of the counterrotating vortex pair through the blade row gives rise to an unsteady pressure distribution on the blade surfaces. The unsteady blade loads generated by this unsteady pressure distribution are significant and will be discussed in the following sections.

#### 5.4 Blade Force And Moment Variations Caused By Convecting Density Wakes

The pressure fluctuations generated by passage of a single sinusoidal density wake can be seen clearly in the Delta  $C_p$  ( $C_p$  suction surface -  $C_p$  pressure

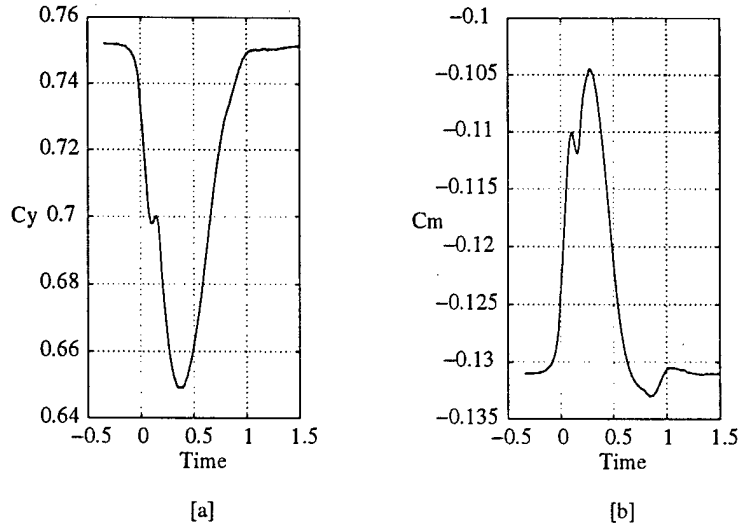


Figure 13: (a) Azimuthal force coefficient  $C_y$  and (b) moment coefficient  $C_m$  (about mid-chord) fluctuation on NACA4F blade during passage of a single sinusoidal density wake,  $\rho^* = -1/3$  and  $w/c = 0.2$ .

surface) vs. time distribution plotted in Figure 12. The local reduction in Delta  $C_p$  convects along the blade following the density wake. As the density wake leaves the blade trailing edge the steady state Delta  $C_p$  distribution is recovered.

The corresponding fluctuation in (a) azimuthal force coefficient  $C_y$  and (b) moment coefficient  $C_m$  is plotted in Figure 13a and Figure 13b respectively. Counterclockwise moments are positive and are calculated about the blade midchord. The wake leading edge encounters the blade row leading edge at  $Time = 0.0$  and leaves the trailing edge of the blade row at  $Time = 1.15$ .

Figure 13a shows a reduction in  $C_y$  as the wake travels over the front of the blade and a subsequent return to steady state as the wake leaves the blade trailing edge. Figure 13b shows an increase in the counterclockwise moment as the wake passes over the front half of the blade. As the wake reaches the blade midchord the moment reverses and decreases back again towards the steady state value.

The counterrotating vortex pair generated across the density wake produce a flux of concentrated fluid which impinges on the blade suction surface. This locally increases the static pressure on the blade suction surface. The corresponding effect on the blade pressure surface is a reduction in static pressure. These two effects combine to reduce the net azimuthal blade force.

A discontinuity, or "bump" occurs on both the  $Cy$  and  $Cm$  curves at  $Time = 0.1$ . This bump occurs as the clockwise vortex at the wake trailing edge passes the leading edge of the blade. The clockwise vortex induces an upwash at the blade leading edge which increase the blade inlet flow angle. This results in an increase in  $Cy$  and a corresponding reduction in  $Cm$ . The magnitude of the upwash diminishes as the clockwise vortex convects past the blade leading edge hence the "bump" is short lived. The size of the discontinuity increases with increasing  $|\rho^*|$  and decreasing  $w/c$ , i.e. with increasing magnitude of the wake density gradient.

The physical nature of the response for wakes with  $\rho^* > 0$  is similar however the fluid flux is now directed toward the blade pressure surface. This results in an initial increase in  $Cy$  and initial decrease in  $Cm$ .

The remaining sections discuss the change in  $\Delta Cy$  ( $Cy(max) - Cy(steady)$ ) and  $\Delta Cm$  ( $Cm(max) - Cm(steady)$ ) for different blade geometries and passage of different density wake distributions.

#### 5.4.1 Flat Top Wakes

The flat top wake tests were conducted to isolate the change in  $\Delta Cy$  and  $\Delta Cm$  caused by changes in wake width. Calculations with the flat top wake were conducted for the NACA4F blade row only. Figure 14 shows the time variation in  $Cy$  and  $Cm$  resulting from the passage of a single flat top density wake with  $\rho^* = 1/9$ . Results for wake widths ranging from  $w/c = 0.0$  to  $w/c = 1.6$  are shown superimposed.

$\Delta Cy$  and  $\Delta Cm$  increases with increasing wake width until a critical width  $w/c \approx 1.3$  (not shown) is reached. Wake widths greater than  $w/c = 1.3$  do not increase the force and moment magnitudes further. An increase in flat top wake width has the effect of moving the counterrotating vortices further apart. For a wake width greater than  $w/c \approx 1.1$ , only one vortex will be contained within the blade row at any given time. The maximum



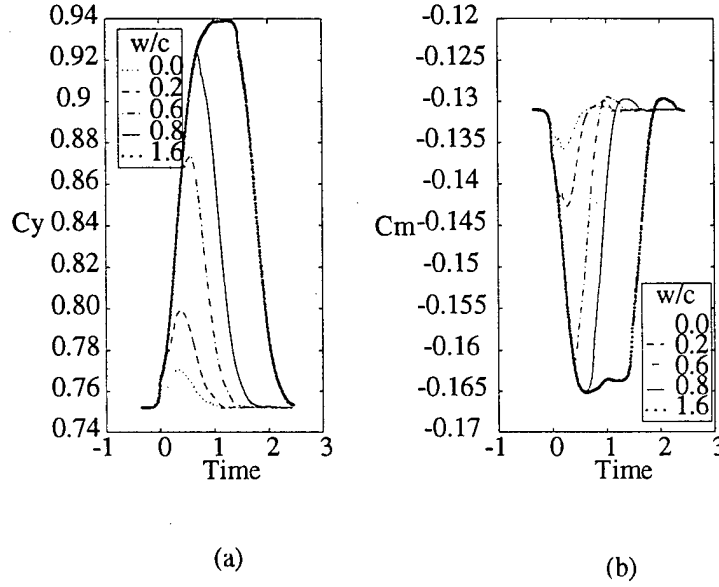


Figure 14: (a) Azimuthal force coefficient  $C_y$  and (b) moment coefficient  $C_m$  (about mid-chord) fluctuation caused by a flat top density wake convecting over the NACA4F blade row.

values of  $C_y$  and  $C_m$  reached at these widths would correspond with Marble's results as applied to a cascade. For wakes with  $w/c > 1.1$ ,  $\Delta C_y$  and  $\Delta C_m$  scale with  $\rho_2/\rho_1$  times  $C_y(steady)$  and  $C_m(steady)$ .

#### 5.4.2 Sinusoidal Wakes

Sinusoidal wake tests were conducted to ascertain the fluctuations in blade  $C_y$  and  $C_m$  during passage of a representative density wake. Calculations were conducted for wake widths  $w/c = 0.1, 0.2$  and  $0.4$  and density changes in the range  $-2/3 < \rho^* < 1/3$  (Table 1).

Figure 15 shows the change in  $\Delta C_y$  and  $\Delta C_m$  during passage of a single sinusoidal wake past the NACA4F blade row. The sinusoidal wake response is similar to the flat top wake response however the rate of change of  $\Delta C_y$  and  $\Delta C_m$  is now dependent upon the wake width. For a given  $\rho^*$ , smaller wake widths imply larger density gradients and hence greater rates of change of  $\Delta C_y$  and  $\Delta C_m$ . The opposite is true for larger wake widths. In addition, the plateau region observed in the flat top wake response (Figure 14) is not

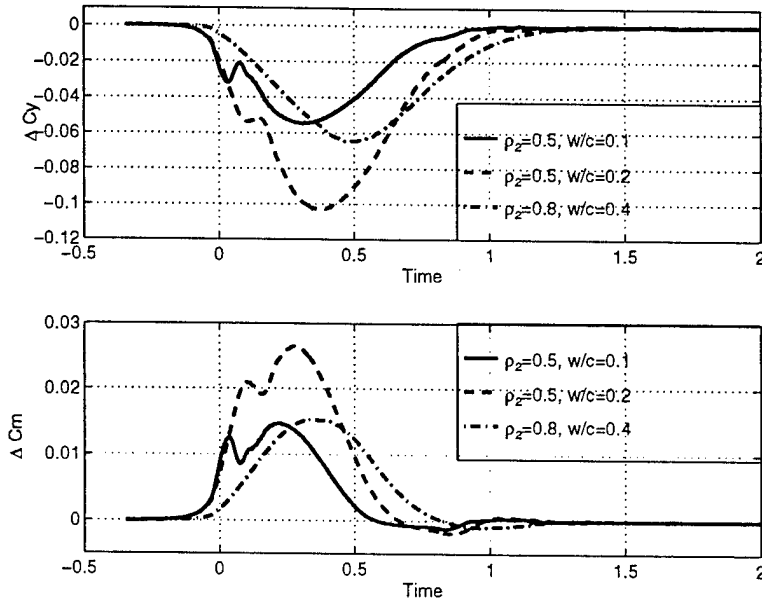


Figure 15: The fluctuation in (a) azimuthal force coefficient  $\Delta C_y$  and (b) moment coefficient  $\Delta C_m$  (about mid-chord) plotted against the convective time scale.

reached. This is because the sinusoidal wake density changes continuously and does not achieve a constant value.

Figure 16 shows  $\Delta C_y$  and  $\Delta C_m$  scaled using  $w/c$  and  $\rho^*$  during passage of several wakes. For small  $w/c$  the curves collapse onto one another (approximately) and confirm use of  $w/c$  and  $\rho^*$  as the relevant scaling parameters.

The change in  $\Delta C_y$  and  $\Delta C_m$  for different values of  $w/c$  and  $\rho^*$  can be more conveniently visualized using the plots in Figure 17 and Figure 18. Results shown here are for wakes convecting past the NACA4F blade row. The curves represent second order polynomial fits to the data. For  $w/c < 0.2$ ,  $\Delta C_y$  and  $\Delta C_m$  scale linearly with  $\rho^*$ . For larger  $w/c$ ,  $\Delta C_y$  and  $\Delta C_m$  deviate gradually from linearity at larger  $|\rho^*|$ .

In the region of interest for a compressor the  $\Delta C_y$  scaling is fairly linear and is given by

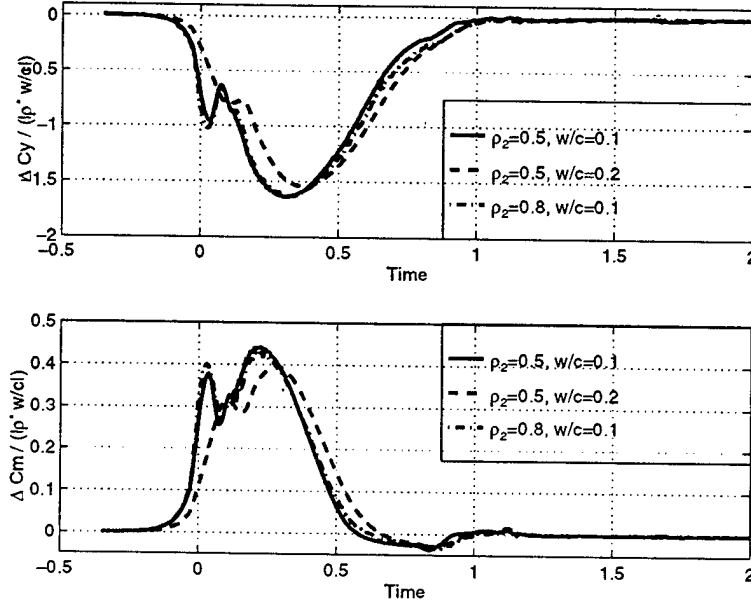


Figure 16: The fluctuation in (a) azimuthal force coefficient  $\Delta C_y$  and (b) moment coefficient  $\Delta C_m$  (about mid-chord) plotted against the convective time scale.

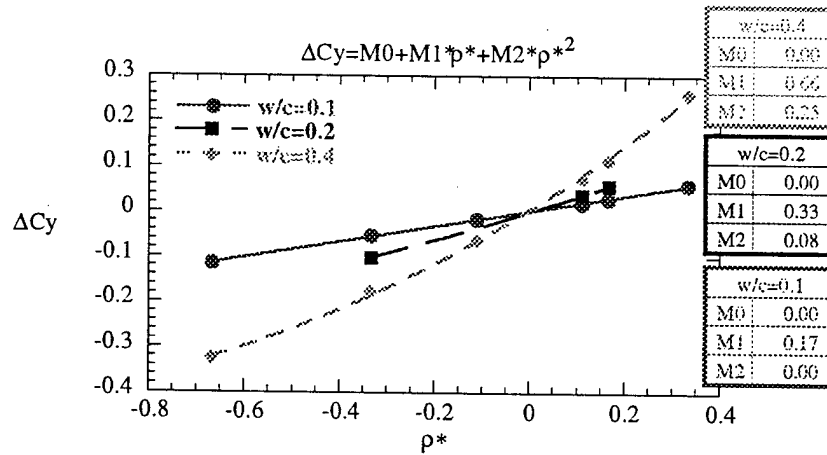


Figure 17: Maximum change in  $C_y$  during passage of a sinusoidal density wake through the NACA4F blade row.

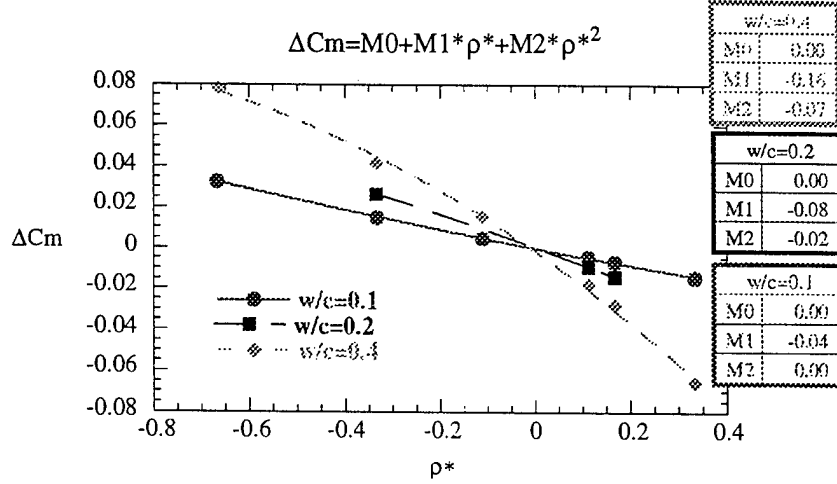


Figure 18: Maximum change in  $C_m$  during passage of a sinusoidal density wake through the NACA4F blade row.

$$\frac{\Delta C_y}{C_{y_{steady}}} = 2.19 \left( \frac{w}{c} \right) \rho^* \quad (4)$$

Similarly the  $\Delta C_m$  scaling is given by

$$\frac{\Delta C_m}{C_{m_{steady}}} = 3.05 \left( \frac{w}{c} \right) \rho^* \quad (5)$$

The change in  $\Delta C_y$  and  $\Delta C_m$  for the EEE blade calculations are shown in Figure 19 and Figure 20. Calculations for two different  $\rho^*$  values were conducted for each wake width,  $w/c = 0.1$  and  $w/c = 0.2$ .

The  $\Delta C_y$  scaling for  $w/c = 0.1$  and  $w/c = 0.2$  are respectively,

$$\frac{\Delta C_y}{C_{y_{steady}}} = 2.34 \left( \frac{w}{c} \right) \rho^* \quad (6)$$

$$\frac{\Delta C_y}{C_{y_{steady}}} = 2.10 \left( \frac{w}{c} \right) \rho^* \quad (7)$$

The constants in the above scaling for  $\Delta C_y$  differ by  $\approx 5\%$  from the constant

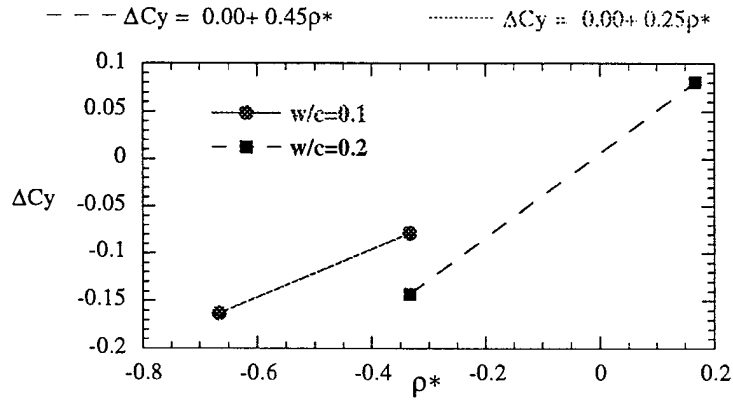


Figure 19: Maximum change in  $C_y$  during passage of a sinusoidal density wake through the EEE blade row.

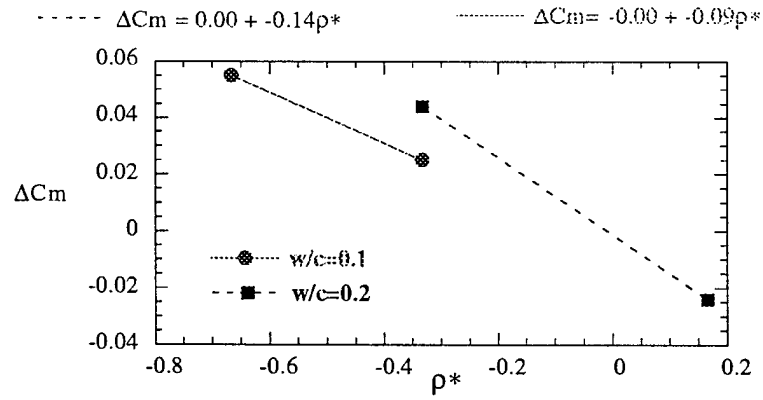


Figure 20: Maximum change in  $C_m$  during passage of a sinusoidal density wake through the EEE blade row.

in the  $\Delta Cy$  expression obtained for the NACA4F blade row.

The moment relations for the EEE blade row for  $w/c = 0.1$  and  $w/c = 0.2$  are respectively,

$$\frac{\Delta Cm}{Cm_{steady}} = 6.45 \left( \frac{w}{c} \right) \rho^* \quad (8)$$

$$\frac{\Delta Cm}{Cm_{steady}} = 5.02 \left( \frac{w}{c} \right) \rho^* \quad (9)$$

The constant in the above scalings for  $\Delta Cm$  differ significantly from the constant in the  $\Delta Cm$  expression obtained for the NACA4F blade row. Better comparison is found if the blade row pressure rise  $\Psi$  is also included in the scaling relations (EEE  $\Psi = 0.5$ , and NACA4F  $\Psi = 0.31$ ), i.e.

$$\frac{\Delta Cm}{\Psi Cm_{steady}} = 9.84 \left( \frac{w}{c} \right) \rho^* \text{ NACA4F blade} \quad (10)$$

$$\frac{\Delta Cm}{\Psi Cm_{steady}} = 12.90 \left( \frac{w}{c} \right) \rho^* \text{ EEE blade, } w/c = 0.1 \quad (11)$$

$$\frac{\Delta Cm}{\Psi Cm_{steady}} = 10.04 \left( \frac{w}{c} \right) \rho^* \text{ EEE blade, } w/c = 0.2 \quad (12)$$

## 5.5 Conclusions Based On Inviscid Results

1. The passage of a density wake through a cascade blade row results in the formation of a pair of convecting counterrotating vortices in the blade passage. For a density wake with density lower than freestream, the counterrotating vortices generate a flux of low density fluid directed towards the blade suction surface. This fluid flux affects the blade pressure distribution and subsequently the force and moment coefficients.
2. The fluctuation in azimuthal force coefficient and moment coefficient during passage of a sinusoidal density wake takes the profile shown in Figure 13. The general shape of this profile is common over the range of wake widths,  $0.1 < w/c < 0.4$ , and density parameters,  $(-2/3 < \rho^* < 1/3)$ .

3. Parametric studies show the maximum fluctuation in blade azimuthal force and moment coefficients are given by:

$$\Delta Cy = f(w/c, \rho^*, Cy(steady))$$

$$\Delta Cm = f(w/c, \rho^*, Cm(steady), \Psi)$$

The effect of blade spacing  $h/c$  (obtained from Equation 3) is believed to be included in the terms  $Cy(steady)$  and  $\Psi Cm(steady)$ .

4. For  $w/c < 0.2$  and  $-0.2 < \rho^* < 0.2$ ,  $\Delta Cy$  and  $\Delta Cm$  scale linearly. Increasing non-linearity is observed for larger  $w/c$  and  $|\rho^*|$ .
5. Factors such as pressure gradient distribution and buoyancy effects may explain differences between the blade loading relations as well as account for the non-linearity in  $\Delta Cy$  and  $\Delta Cm$  at higher  $w/c$  and  $|\rho^*|$ .

## 6 Viscous Flow Results

The effect of viscosity on density wake induced blade force and moment fluctuations was determined for freestream Mach numbers  $M_\infty = 0.15$  and  $M_\infty = 0.53$ . The maximum changes in blade force and moment coefficients are compared for different wake  $w/c$  and  $\rho^*$  just as in the inviscid case. The shapes of the inviscid and viscous blade force and moment profiles is also compared. A physical argument based on flow field features is presented to explain the observed differences.

Before continuing with the viscous results, a brief description of the viscous flow solver and computational grid is presented.

### 6.1 Viscous Flow Solver

An unsteady two-dimensional viscous flow solver written by Hoying [3] is used to solve the Navier Stokes flow equations. Primary features of this solver are,

1. Finite difference discretization.
2. Fourth-order spatial accuracy and third-order temporal accuracy.
3. Dispersion Relation Preserving (DRP) scheme (Tam and Web [11]).
4.  $\kappa - \epsilon$  turbulence model with wall functions (Chieng and Launder [1]).
5. Non-reflecting inlet and exit boundary conditions (Giles [2]).

The merit of an unsteady flow solver lies in its ability to capture and propagate high wave numbers at the correct speeds. The Dispersion Relation Preserving scheme used in this solver has the advantage of optimizing the dissipation and dispersion characteristics of the finite difference method over a large number of wavelengths than say a four-stage Runge-Kutta scheme [3]. The resulting high-order scheme reduces the computational cost by requiring fewer grid points.

Additional computational savings are achieved by using wall functions to model the inner portion of the blade boundary layers. This allows considerable reduction of the number of near wall grid points.



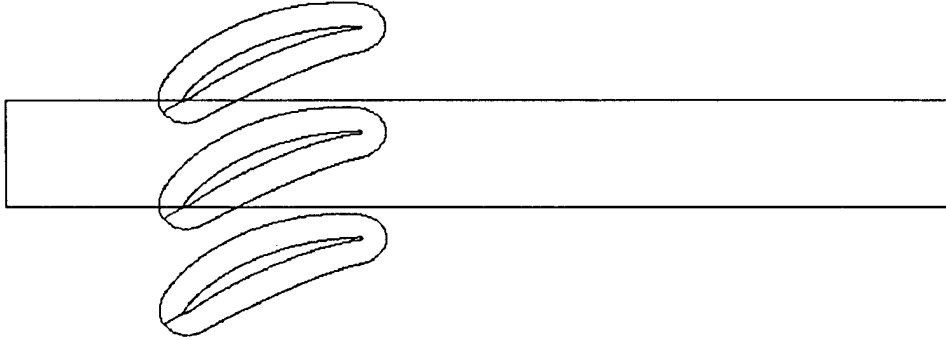


Figure 21: Overlapping H grid (along the duct) and O grids (around the blades) used for the viscous calculation.

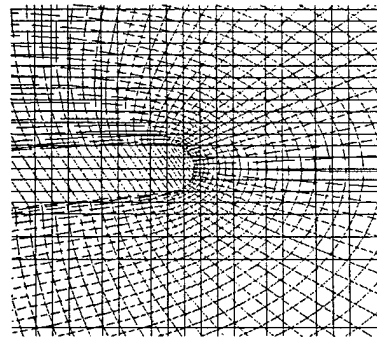
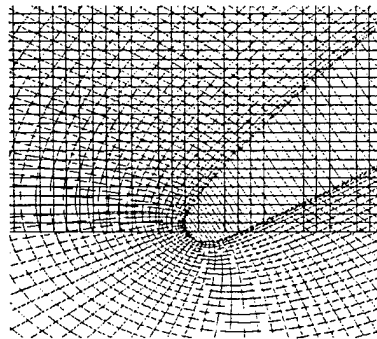


Figure 22: Grid detail near the blade leading edge and blade trailing edge regions.

Property	Inviscid	Viscous
$Re_\infty$	-	623217
Mach No.	0	0.15
Blade row pressure rise $\Psi$	0.50	0.46
Blade stagger (degrees)	45	24
Blade profile	EEE	EEE

Table 2: Comparison of inviscid and viscous flow conditions ( $Re_\infty$  is based on blade chord and inlet total velocity).

Convective time scale	Location of density wake
0.0	wake l.e. intercepts blade l.e.
0.1	wake t.e. intercepts blade l.e.
1.3	wake t.e. passes blade t.e.

Table 3: Location of density wake at different times for  $M_\infty = 0.15$  calculation.

The computational grid used in this study consists of overlapping H-grids and O-grids as show in Figure 21 and Figure 22. Subsonic inflow and outflow boundary conditions are imposed at the inlet and exit planes of the computational domain while periodic boundary conditions are used along the duct edges.

The flow in the ducts is assumed to be governed almost exclusively by inviscid relations hence the H-grid region is computed solely by the Euler equation. The Navier–Stokes equations are solved in the O-grid region surrounding the blades. An elliptic partial differential equation method was used to generate the O-grid using methods presented by Steger and Sorenson [9].

For a detail description of the numerical discretization and grid generation procedures refer to Hoying [3].

## 6.2 Comparison of Inviscid and Viscous Results

A comparison of the flow and geometry features of the inviscid and viscous calculation is listed in Table 2.

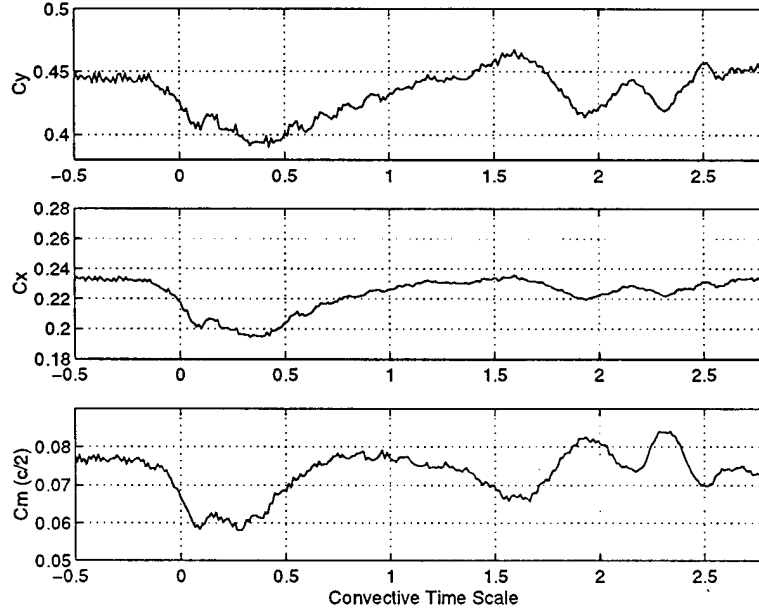


Figure 23: Force and moment coefficient fluctuation during passage of a wake width  $w/c = 0.2$  and  $\rho^* = -1/3$ ,  $M_\infty = 0.15$ . Convective time scale=0.0 corresponds to the wake i.e. intercepting the blade i.e.

The viscous results for blade force and moment fluctuation during passage of a density wake of width  $w/c = 0.2$  and  $\rho^* = -1/3$  is shown in Figure 23. Counterclockwise moments are defined negative in the viscous solver and are calculated about the blade midchord. Table 3 lists the approximate location of the density wake at different times.

The force and moment coefficients respond before the density wake intercepts the blade leading edge. This feature is also observed in the inviscid results and is a consequence of the downwash field associated with the counterrotating vortices. The slight jump in the force and moment coefficients as the wake trailing edge passes over the blade leading edge is also another common feature.

The shape of the viscous force and moment profiles are similar to the inviscid profiles for  $Time < 1.3$ . Unlike the inviscid results however the viscous results show continued blade force and moment fluctuation for  $Time > 1.3$  after the density wake leaves the blade row trailing edge. The additional un-

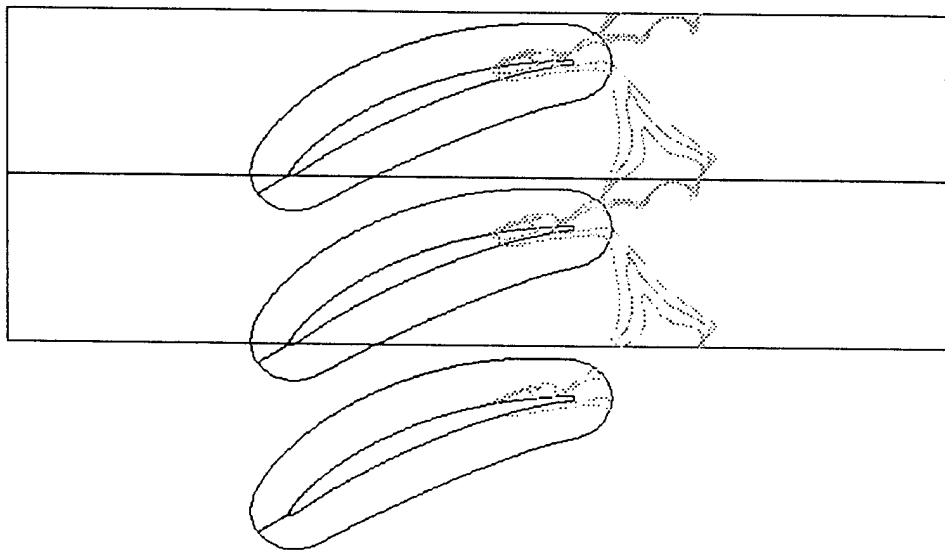


Figure 24: Density contours indicating location of trapped wake fluid at  $Time = 1.54$ .

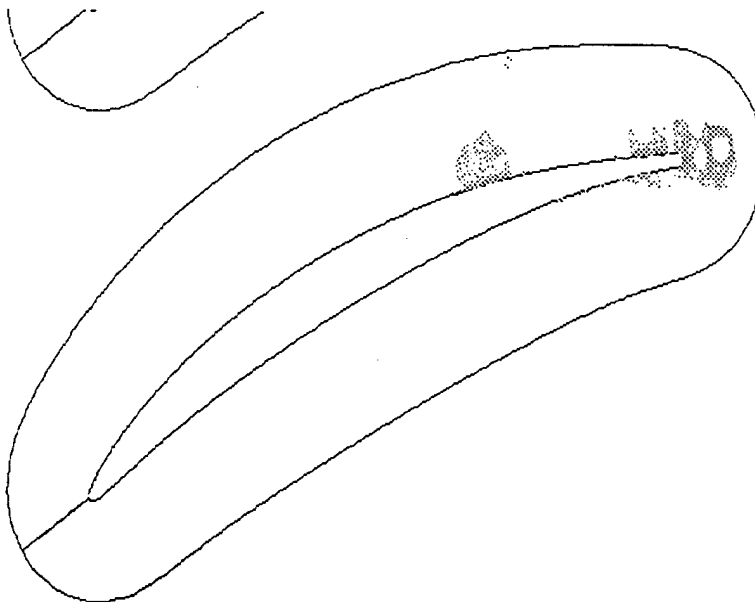


Figure 25: Perturbation static pressure contours showing location of localized low pressure region at  $Time = 1.05$ .

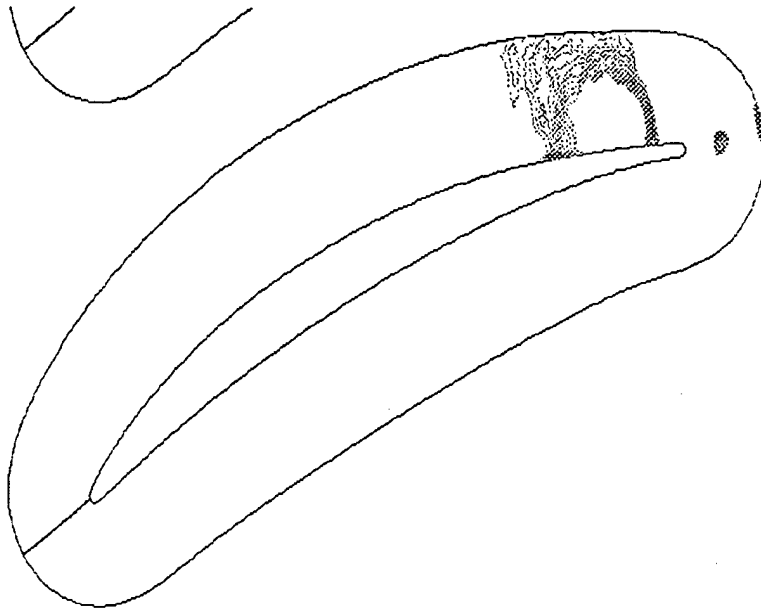


Figure 26: Perturbation static pressure contours showing location of localized low pressure region at  $Time = 1.54$ .

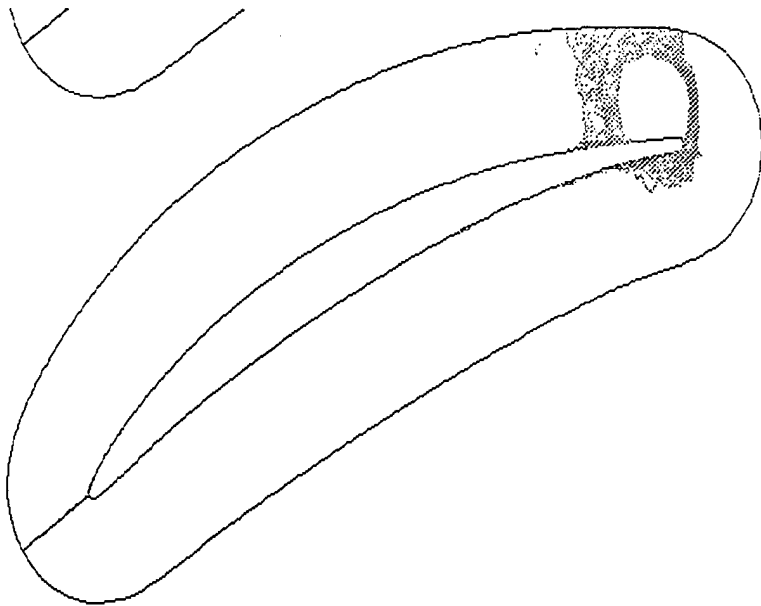


Figure 27: Perturbation static pressure contours showing location of localized low pressure region at  $Time = 1.76$ .

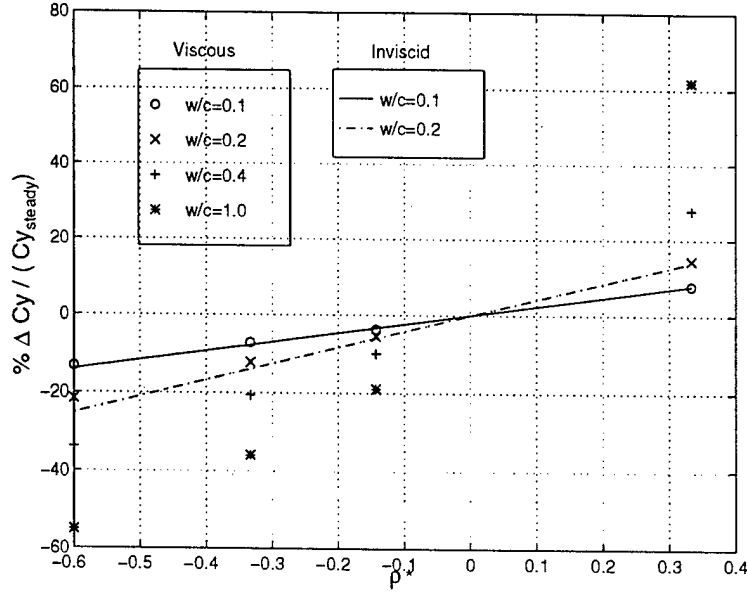


Figure 28: Comparison of inviscid and viscous results ( $M_\infty = 0.15$ ) for maximum change in blade azimuthal force coefficient.

steadiness is a result of a low pressure recirculating region which consists of low density wake fluid. This low density fluid is trapped in the trailing edge region of the suction surface boundary layer behind the convecting density wake (see Figure 24). The development of the low pressure region can be seen from the perturbation pressure contour plots of Figure 25 through Figure 27. The recirculating region first appears at  $Time \approx 0.7$  and is formed as the blade boundary layer deforms under the perturbation velocity field of the counterrotating vortex pairs. As the density wake leaves the blade row the recirculating region convects towards the blade trailing edge.

The localized low pressure region decays as the density wake convects downstream and the blade boundary layer re-develops. The time required for force fluctuations to diminish could not be determined from this calculation because of numerical instability caused as the density wake passed through the exit plane of the computational domain. Blade force fluctuations were observed even after the density wake had passed 3 chord lengths ( $\equiv 1$  computational domain length) downstream.

The maximum change in the blade force and moment coefficients ( $\Delta C_y$ ,

Steady		$C_y = 0.44$	$C_m = 0.08$	$C_x = 0.23$
Uncertainty		$\pm 1\%$	$\pm 2\%$	$\pm 1\%$
$w/c$	$\rho_2/\rho_1$	$\% \Delta C_y$	$\% \Delta C_m$	$\% \Delta C_x$
0.1	0.25	-13	-27	-18
	0.50	-7	-15	-10
	0.75	-4	-7	-4
	2.00	+8	+13	+9
0.2	0.25	-22	-44	-30
	0.50	-12	-25	-17
	0.75	-6	-12	-8
	2.00	+15	+25	+19
0.4	0.25	-34	-64	-46
	0.50	-21	-38	-27
	0.75	-10	-19	-14
	2.00	+28	+56	+40
1.0	0.25	-55	-84	-71
	0.50	-36	-55	-46
	0.75	-19	-27	-23
	2.00	+62	+95	+80

Table 4: Maximum change in azimuthal force coefficient and moment coefficient for  $M_\infty = 0.15$  viscous calculation.

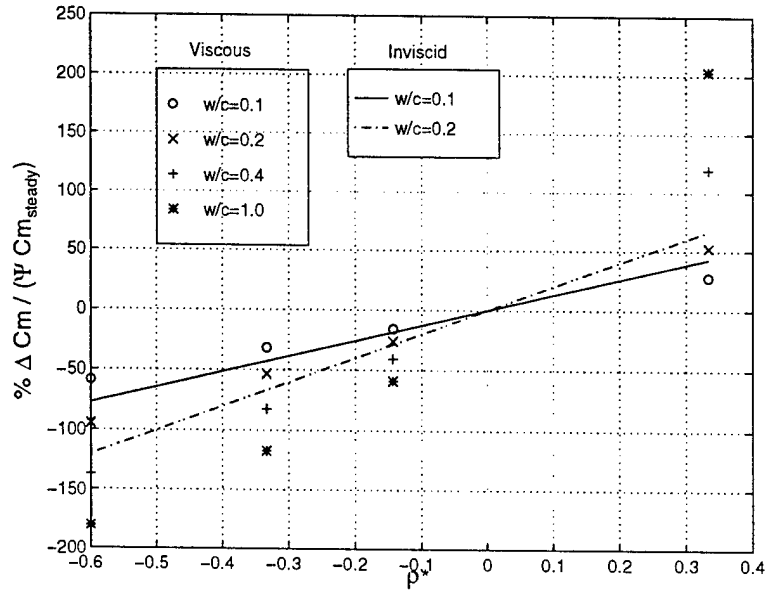


Figure 29: Comparison of inviscid and viscous results ( $M_\infty = 0.15$ ) for maximum change in blade moment coefficient about mid-chord.

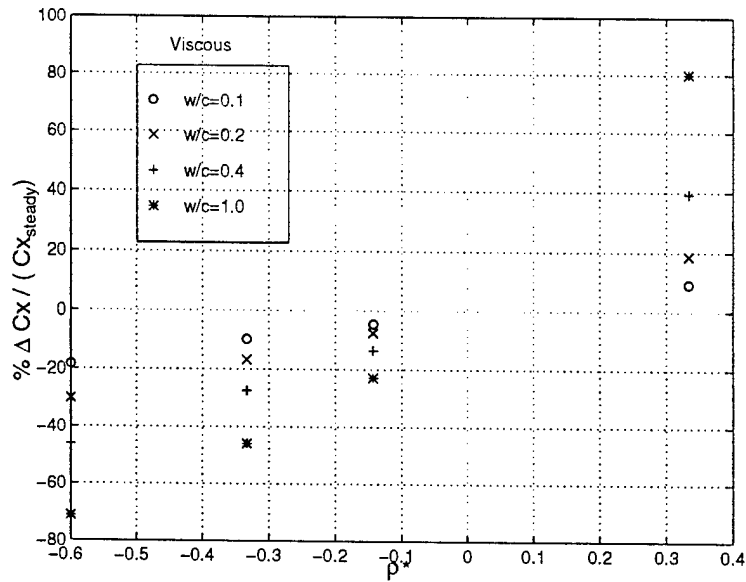


Figure 30: Viscous results ( $M_\infty = 0.15$ ) for maximum change in blade axial force coefficient.



Convective time scale	Location of density wake
0.0	wake l.e. intercepts blade l.e.
0.2	wake t.e. intercepts blade l.e.
1.4	wake t.e. passes blade t.e.

Table 5: Location of density wake at different times for  $M_\infty = 0.53$  calculation.

$\Delta Cm$ ,  $\Delta Cx$ ) for the  $M_\infty = 0.15$  calculation are listed in Table 4 for a range of wake properties. A comparison of these maximum changes with the corresponding inviscid results is shown in Figure 28 and Figure 29. These plots show the change in force and moment coefficients normalized by the steady force and moment coefficient and the blade row pressure rise coefficient  $\Psi$ . In addition Figure 30 shows the maximum change in the viscous axial force coefficient.

The inviscid and viscous results for  $\Delta Cy$  compare well for wake widths  $w/c = 0.1$  and  $w/c = 0.2$ . The inviscid  $\Delta Cm >$  viscous  $\Delta Cm$  over the complete range of  $\rho^*$ . The difference between the inviscid and viscous values is also seen to increase with  $|\rho^*|$ . In particular the moment coefficients are seen to differ greatly at large  $|\rho^*|$ . These differences are still under investigation. The influence of boundary layer parameters (momentum thickness, boundary layer thickness, Reynolds number) on these differences is also being addressed.

### 6.3 Comparison of Incompressible and Compressible Results

The force and moment coefficient profiles during passage of a density wake of width  $w/c = 0.2$  and  $\rho^* = -1/3$  at freestream  $M_\infty = 0.53$  (compressible but no shock waves) is shown in Figure 31. Table 5 lists the location of the density wake at different times.

$\Delta Cy$ ,  $\Delta Cm$  and  $\Delta Cx$  for the compressible calculation is listed in Table 6 and compared with the viscous results in Figure 32 through Figure 34.

The compressible results show greater unsteadiness than the corresponding incompressible results. Note the effects of compressibility are much greater for  $\rho^* > 0$  compared with  $\rho^* < 0$ . The unsteadiness in force and

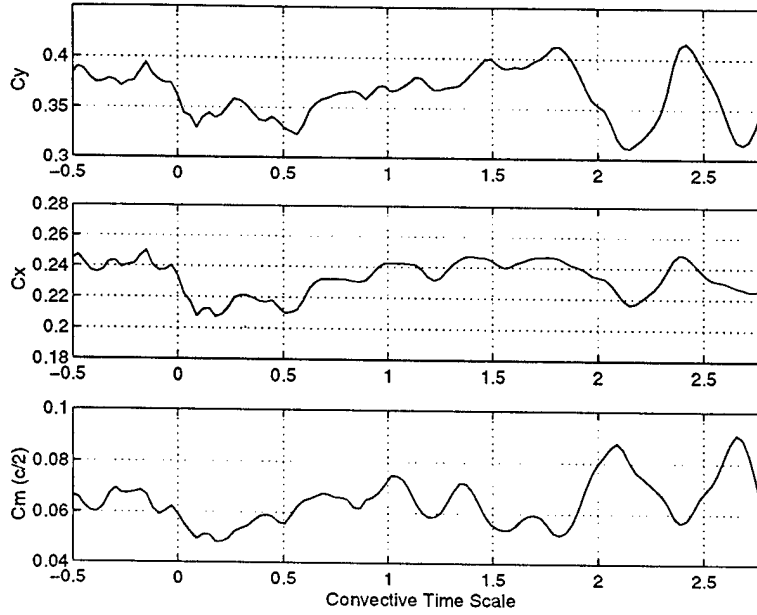


Figure 31: Force and moment coefficient fluctuation during passage of a wake width  $w/c = 0.2$  and  $\rho^* = -1/3$ ,  $M_\infty = 0.53$ .

Steady		$Cy = 0.38$	$Cm = 0.07$	$Cx = 0.24$
Uncertainty		$\pm 3\%$	$\pm 7\%$	$\pm 3\%$
$w/c$	$\rho_2/\rho_1$	$\% \Delta Cy$	$\% \Delta Cm$	$\% \Delta Cx$
0.1	0.25	-14	-29	-14
	0.50	-8	-16	-7
	0.75	-3	-13	-4
	2.00	+11	+29	+16
0.2	0.25	-24	-40	-24
	0.50	-15	-27	-13
	0.75	-8	-17	-7
	2.00	+20	+55	+26
0.4	0.25	-34	-64	-38
	0.50	-21	-38	-22
	0.75	-11	-24	-11
	2.00	+36	+63	+41

Table 6: Results for  $M_\infty = 0.53$  viscous calculation. Percentage change from mean of maximum blade force and moment coefficients.

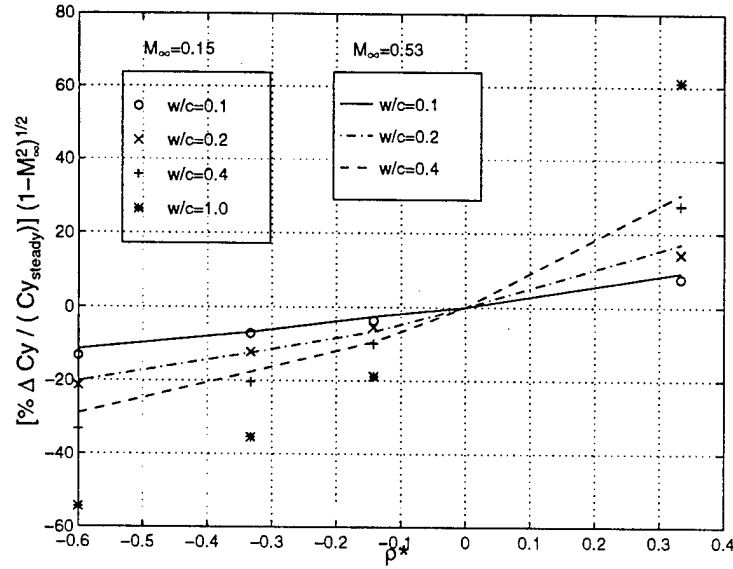


Figure 32: Comparison of the incompressible ( $M_\infty = 0.15$ ) and compressible ( $M_\infty = 0.53$ ) maximum change in blade azimuthal force coefficient.

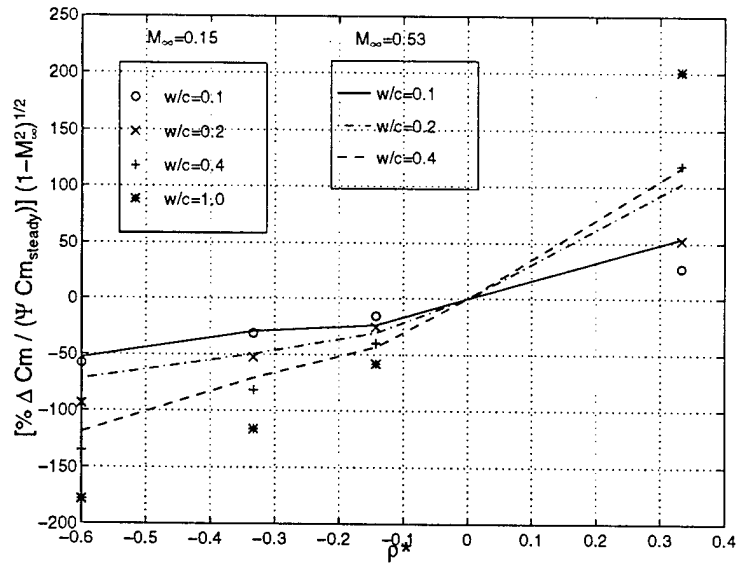


Figure 33: Comparison of the incompressible ( $M_\infty = 0.15$ ) and compressible ( $M_\infty = 0.53$ ) maximum change in blade moment coefficients.

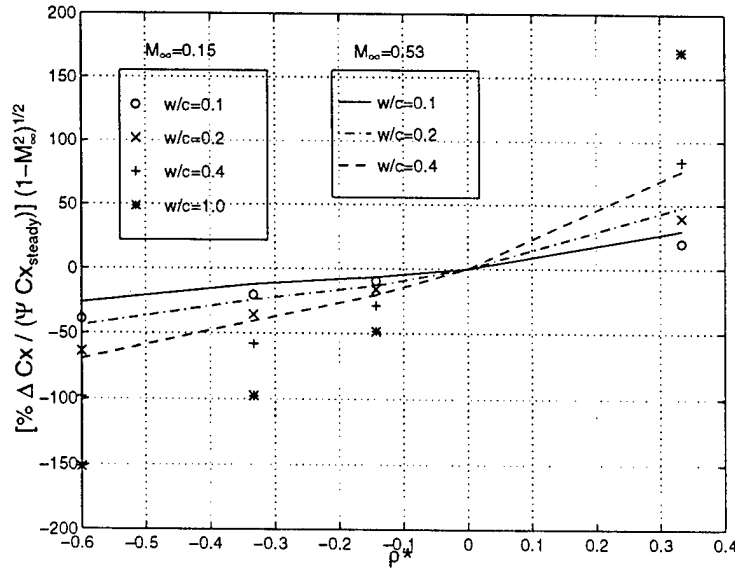


Figure 34: Comparison of the incompressible ( $M_\infty = 0.15$ ) and compressible ( $M_\infty = 0.53$ ) maximum change in blade axial force coefficients.

moment coefficients after the density wake leaves the blade trailing edge is also greatly enhanced. While the source of this increased unsteadiness is still under investigation, the effect of compressibility to increase the fluctuating loads is clear. The implication of this is important to the larger problem of coupled aeroelastic motion and induced strain.

#### 6.4 Conclusions Based On Viscous Results

1. The inviscid and viscous force and moment fluctuation profiles are comparable for times prior to the density wake leaving the blade row trailing edge. The profiles share similar qualitative features, i.e. the response begins before the density wake intercepts the blade leading edge and the "bump" in the profiles occur as the wake trailing edge passes the blade leading edge.
2. The viscous results show continued blade force and moment fluctuations after the density wake leaves the blade row trailing edge. These fluctuations are attributed to the development of a low pressure region which consists of density wake fluid trapped in the suction surface boundary layer. Calculations at  $M = 0.53$  show increased amplitude of

these fluctuations (sometimes greater than the initial response) compared to  $M = 0.15$ . In addition this trapped wake fluid seems to interfere with the formation of trailing edge vortices.

3. Parametric results show good comparison between the inviscid and viscous maximum change in force and moment coefficients for the ranges  $w/c < 0.2$  and  $-0.2 < \rho^* < 0.2$ . Larger deviations are seen with increasing  $|\rho^*|$ . In particular the results for  $\rho^* > 0$  show significant deviations. Additional scaling terms for this region are under investigation.

## 7 Further Work

The following research objectives are expected to be reached during the nine month interval from January 1, 1998 to September 30, 1998.

1. Clarification of the physics and quantitative assessment of the blade force and moment fluctuations after the density wake leaves the blade row trailing edge.
2. Determine additional scaling parameters for maximum blade force and moment fluctuations at larger  $|\rho^*|$ .
3. Perform calculations at higher Mach Nos. ( $> 1.0$ ) to determine shock wave - density wake interaction.
4. Perform laminar flow calculation at lower Reynolds number.

## 8 Acknowledgments

This work has been supported by the Air Force Office of Scientific Research and supervised by Major Brian Sanders, Program Manager, under contract number F49620-94-1-0202. This support is gratefully acknowledged. We are also grateful to Prof. Frank Marble of CalTech whose original work motivated this study and who provided many useful discussions.

## References

- [1] Chieng, C. C. and Launder, B. E., "On the Calculation of Turbulent Heat Transport Downstream from an Abrupt Pipe Expansion." *Numerical Heat Transfer*. Vol. 3. 1980. 189-207.
- [2] Giles, M. B., *Non-Reflecting Boundary Conditions for the Euler Equations*. CFDL-TR-88-1. Computational Fluid Dynamics Laboratory, Massachusetts Institute of Technology. February 1988.
- [3] Hoying, D. A., *Blade passage Flow Structure Effects On Axial Compressor Rotating Stall Inception*. PhD. Thesis, Massachusetts Institute of Technology, Department of Aeronautics and Astronautics. September 1996.
- [4] Kemp, N. H. and Sears, W. R., "The Unsteady Forces Due to Viscous Wakes in Turbomachines." *Journal of Aeronautical Sciences*. Vol.22, No.7. July, 1955. 478-483.
- [5] Kerrebrock, J. L. and Mikolajczak, A. A., "Intra-Stator Transport of Rotor Wakes and its Effect on Compressor Performance." ASME Paper 70-GT-39. 1970.
- [6] Manwaring, S. R. and Wisler, D. C., "Unsteady Aerodynamics and Gust Response in Compressors and Turbines." ASME Paper 92-GT-422. 1992.
- [7] Marble, F. E., "Response of a Thin Airfoil Encountering a Strong Density Discontinuity." *Journal of Fluids Engineering*. Vol. 115. Dec. 1993. 580-589.
- [8] Ramer, B. E., *Aerodynamic Response of Turbomachinery Blade Rows to Convecting Density Distortions*. S.M. Thesis, Massachusetts Institute of Technology, Department of Aeronautics and Astronautics. December 1996.
- [9] Steger, J. L. and Sorenson, R. L., "Automatic Mesh-Point Clustering Near a Boundary in Grid Generation with Elliptic Partial Differential Equations." *Journal of Computational Physics*. Vol. 33. 1979. 405-410.
- [10] Ramer, B. E., Wijesinghe, H. S., Tan, C. S., Covert, E. E., "Aerodynamic Response of Turbomachinery Blade Rows to Convecting Density Wakes." AD-VOL.55. Proceedings of the ASME Aerospace Division.

Presented at the International Mechanical Engineering Congress and Exposition, Dallas, Texas. November, 1977.

- [11] Tam, C. K. W. and Webb J. C., "Dispersion-Relation-Preserving Finite Difference Schemes for Computational Acoustics." *Journal of Computational Physics*. Vol 107. 1993. 262-281.
- [12] Valkov, Theodore V., *Control of Unsteady Flow in a Stator Blade Row Interacting with Upstream Moving Wakes*. S.M. Thesis, Massachusetts Institute of Technology, Department of Aeronautics and Astronautics. Also GTL Report No. 255. May 1992.
- [13] Wisler, D. C., *Core Compressor Exit Stage Study, Volume I - Design Report*. NASA CR-135391. NASA Lewis Research Center. December 1977.